Range profiles of 25—100-keV neon ions in eleven elemental solids

R. Lappalainen
Accelerator Laboratory, University of Helsinki, Siltavuorenpenger 20 M, SF-00170 Helsinki, Finland
(Received 24 February 1986)

The depth profiles of 25—100-keV $^{20}Ne^+$ and $^{22}Ne^+$ ions implanted into C, Si, V, Co, Ni, Zr, Nb, Ag, Hf, W, and Au backings have been measured with the (p,γ) resonance broadening technique. The modal, mean, and standard-deviation values were determined for the range profiles extracted from the measured γ-ray yield curves. The theoretical predictions were calculated with the computer-simulation code COSIPO for both amorphous and polycrystalline structures. The experimental modal ranges corrected for sputtering agree within error limits ($\lesssim 10\%$) with the ranges calculated, assuming an amorphous structure for the backing. The measured mean ranges are longer than theoretical values for an amorphous structure by a factor of 1.1—1.3. However, the mean range predictions for a polycrystalline structure are generally closer to the experimental ones, although the shapes of profiles are somewhat different.

I. INTRODUCTION

The experimental range-distribution data of low-energy ions is of current interest both for testing theoretical models and for many important applications, e.g., in metallurgy and in the fabrication of integrated circuits. Discrepancies existing between experimental results and theoretical calculations[1] are attributed mainly to uncertainty in the electronic stopping power and to effects of the crystal structure of targets, generally excluded in the calculations. The importance of these effects has been illustrated by Monte Carlo simulations, e.g., Refs. 2 and 3. However, to date, only a few systematic range-profile measurements for low-energy light ions in different backings have been reported (e.g., references in Refs. 1 and 4), evidently due to the lack of suitable subsurface probing methods. The nuclear resonance broadening (NRB) method,[5,6] requiring a low-energy ($\lesssim 2.0$ MeV) accelerator, has proved its suitability for depth profiling of almost all light elements, especially when they are in heavy backings.

In our laboratory, the systematic studies of the low-energy range profiles in different backing materials have been carried out earlier for nitrogen[7,8] and aluminum.[9] In the present work, the projectile systematics were extended to the chemically inactive gas, neon. The NRB method is well suited to probe for neon because of the narrow, isolated (p,γ) resonances of neon isotopes. The conventional backscattering method cannot be used for accurate profiling of neon, nor for light elements in general, since the atomic mass of the implant is less than that of most backings. Secondary-ion mass spectrometry (SIMS) can be used to measure only large concentrations of light inert gases because of the low ionization probability for these elements. Furthermore, as Eichinger and Ryssel pointed out in their recent comparison of several measuring techniques,[10] the intrinsic difficulties of SIMS make it semiquantitative for its general application. In certain special cases, other nuclear reaction methods such as activation, particle reactions, or scattering can be utilized but the depth resolution of these methods is normally less than that of the NRB method with γ-ray detection.

The aim of the present work is to study the range distributions of neon in relevantly selected elemental backings, i.e., in elements with high melting points and which cover the Z_2 region appropriately spaced. An additional aim is to study the effect of target structure by comparison of the experimental results and Monte Carlo simulations for amorphous, random, and polycrystalline targets. The main features of the measurement technique, analysis of the experimental data, and computer simulations are described briefly in the corresponding sections. The results are compared with theoretical profiles in graphs and using the statistical characteristics of the distributions. Finally, possible reasons for differences between experimental and theoretical results are discussed.

II. MEASUREMENTS

The NRB method requires that an isotope of the element to be analyzed have an isolated, narrow resonance in the nuclear-reaction cross section. In the case of neon, there are three stable isotopes; ^{20}Ne, ^{21}Ne, and ^{22}Ne, with natural abundances of 90.51, 0.27, and 9.22%, respectively. ^{20}Ne has only one useful, well-isolated (p,γ) resonance, at $E_p=1169$ keV [$\Gamma=16$ eV, $(2J+1)\Gamma_p\Gamma_\gamma/\Gamma=1.6\pm0.3$ eV, $E_\gamma=3.54$ MeV (96%)].[11] $^{21}Ne(p,\gamma)$ resonances are rather broad, typically 3—4 keV, and not well known. No suitable resonance exists in the useful proton energy range.[11] On the other hand, ^{22}Ne possesses several strong, narrow (p,γ) resonances even at bombarding energies below 1 MeV, e.g., at $E_p=640$, 851, and 950 keV.[11] The resonance at $E_p=851.4\pm0.7$ keV [$\Gamma=6$ eV, $(2J+1)\Gamma_p\Gamma_\gamma/\Gamma=12$ eV] is most frequently used. Due to the relatively low proton energy needed and the strong, high-energy ($E_\gamma>9$ MeV) primary γ radiation of $^{22}Ne(p,\gamma)$ resonances, the γ-ray yield of a suitably chosen resonance can be resolved from the background rather well even with light backings, such as C, Si, and V.

For the selection of backing materials, elements with high melting points were preferred in order to avoid er-

roneous profiles due to diffusion or significant sputtering of the surface during implantation.[12] In addition, high-sputtering-factor materials Ag and Au were included since they are frequently used backings in range and stopping-power measurements. The backings, i.e., C, Si, V, Co, Ni, Zr, Nb, Ag, Hf, W, and Au were commercially available grade plates with thickness 0.3–1 mm. Their purities were better than 99.8%, except for Hf, which contained about 3 at. % Zr. Silicon samples were 1-mm-thick, float-zoned p-type (111) silicon wafers. The neon-implanted samples were prepared using the electromagnetic isotope separator of the laboratory. The samples were implanted to doses ranging from 6×10^{14} to 6×10^{16} ions/cm^2 with energies of 25, 50, 75, and 100 keV. ^{20}Ne ions were used for heavy backings, i.e., Co, Ni, Zr, Nb, Ag, Hf, W, and Au. Because of the disturbing low-energy background radiation, ^{22}Ne was used for the light elements C, Si, and V.

Neon implantation profiles were measured using the 2.5-MV Van de Graaff accelerator at the laboratory. The (p,γ) resonance at $E_p=1169$ keV was used for ^{20}Ne and the 640- and 851-keV resonances were utilized for ^{22}Ne. The γ rays from a resonance were detected either with a 12.7×10.2-cm^2 NaI(Tl) crystal or with a Princeton gamma-tech 110-cm^3 Ge(Li) detector. The latter was specifically used to check the background subtraction of the yield curves measured with the NaI detector. The energy resolution of the proton beam (full width at half maximum) on the 4×4 mm^2 spot was about 600 eV, which corresponds typically to a depth resolution of about 4 nm at the surface. The stability of the proton-energy calibration, determining the location of the surface, was checked before and after each series of measurements by measuring a yield curve of a very thin ^{20}Ne or ^{22}Ne target implanted (at 1–2.5 keV) into a Ta backing.

In order to achieve sufficient statistical precision (typically better than 1.6% in the maximum of a γ-ray-yield profile), rather high beam currents had to be used. Therefore, the samples were cooled with liquid nitrogen to prevent excessive heating of the surface. Each profile was measured at least twice to ensure that no significant changes in the implanted profile or surface contamination occurred during the measurements. It turned out that most of the samples could withstand a proton beam of even 10 μA and, e.g., the effects of normal thermal diffusion and radiation-enhanced diffusion were within statistical errors, as evidenced by the reproducibility. On the other hand, the probing proton beam was observed to form blisters in Ag and W backings. Therefore, the yield curves were measured using several spots on the same homogeneous sample area and so good reproducibility was achieved.

III. ANALYSIS OF EXPERIMENTAL DATA

A series of γ-ray yield curves for ^{22}Ne-implanted vanadium is shown in Fig. 1. In the case of the sharp resonance and good energy resolution, the measured yield curve corresponds quite well in shape to the actual concentration distribution of the implanted atoms near the surface. Deeper in the target, the depth resolution of the

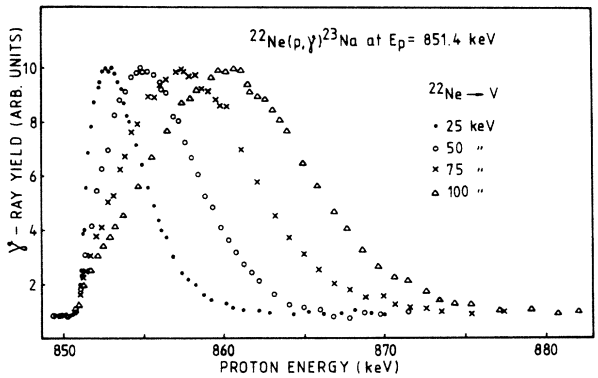

FIG. 1. The γ-ray yield curves from the $^{22}Ne^+$ implantations into vanadium backings. The peak heights are normalized to the same value. The maximum yields were 3000–5000 counts for a proton charge of 30 μC accumulated at each point.

method diminishes as the square root of the depth, due to the energy straggling of the probing proton beam. Thus, in deducing the detailed shapes of the actual concentration profiles, straggling, beam-energy resolution and resonance width have to be taken into account.

The neon profiles were derived from the yield curves using computer programs,[13] which take into account the effect of proton energy straggling on the basis of Vavilov's theory.[14,15] With these interactive programs, concentration profiles are obtained either with an iterative algorithm without any assumptions of the functional form of the profile, or by searching out the best parameters for a certain function by a least-squares fit to the experimental data. In the present work, a split-Gaussian distribution was assumed for the implanted concentration profile.[16] The distribution consists of two half Gaussians with standard deviations σ_- and σ_+ joined at the modal projected range $\hat{R}$. The subscripts $-$ and $+$ refer, respectively, to the left and the right half of the distribution. As an example of the effect of straggling, the observed γ-ray yield curve and the calculated concentration distribution of ^{22}Ne atoms for a 100-keV implantation in V are displayed in Fig. 2. At the implantation energies used in the present work, the correction in width of the measured profile due to proton straggling is typically less than 15%. The proton-stopping-power values used in the analysis were taken from the compilations by Andersen and Ziegler.[17] The change of the proton stopping power in the backing due to the implanted atoms was included in the calculation of the depth scales of the experimental profiles. This effect was always less than 2% for the modal values of the experimental distributions.

IV. RESULTS AND CALCULATIONS

The three parameters of the split-Gaussian distribution $\hat{R}$, σ_-, and σ_+ were determined for all measured profiles by performing a least-squares fit of the calculated yield curve to the background-subtracted measured yield curve.

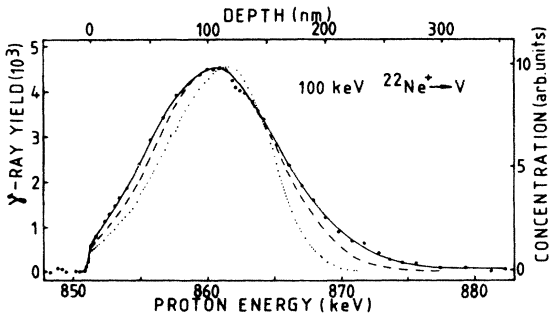

FIG. 2. The measured γ-ray yield and the concentration distribution for 100-keV ^{22}Ne implantation in vanadium. The solid line is the γ yield calculated for the optimized split-Gaussian concentration profile (dashed line). The dotted line is the Monte Carlo simulation for amorphous backing.

It turned out that, in general, the yield curves corresponding to the optimized split Gaussians fitted quite well to the measured profiles. However, especially in the case of tungsten, the calculated fit seemed to have a systematic tendency to undershoot the measured curve somewhat in the tail part of a profile. The normalized split-Gaussian concentration distributions are shown in Fig. 3. The experimental range parameters, i.e., modal, mean, and standard-deviation values of the distributions, are compared with theoretical predictions in Tables I and II. Here, the mean value and the standard deviation are defined to be the first moment and the square root of the second moment, respectively, calculated over the positive depth values of the distribution. For the conversion of range values in units $\mu g/cm^2$, the densities used for backings are included in Table II.

A. Computer simulation of the range distributions

The theoretical range profiles were calculated by the computer simulation program COSIPO (Ref. 2) for both amorphous and polycrystalline backings. For comparison, results using the simple analytical algorithm PRAL by Biersack[18] are also included. COSIPO takes proper account of the reflection of particles at the surface. In the present simulations scattering angles were calculated using a "mean" of the potentials based on the Gordon-Kim approximation and the Dirac-Fock electron distributions.[19] The so-called binary-collision approximation was used and thermal vibration of atoms in crystal was included.

The target structures utilized in the simulations are amorphous, polycrystalline (the crystal is rotated random-

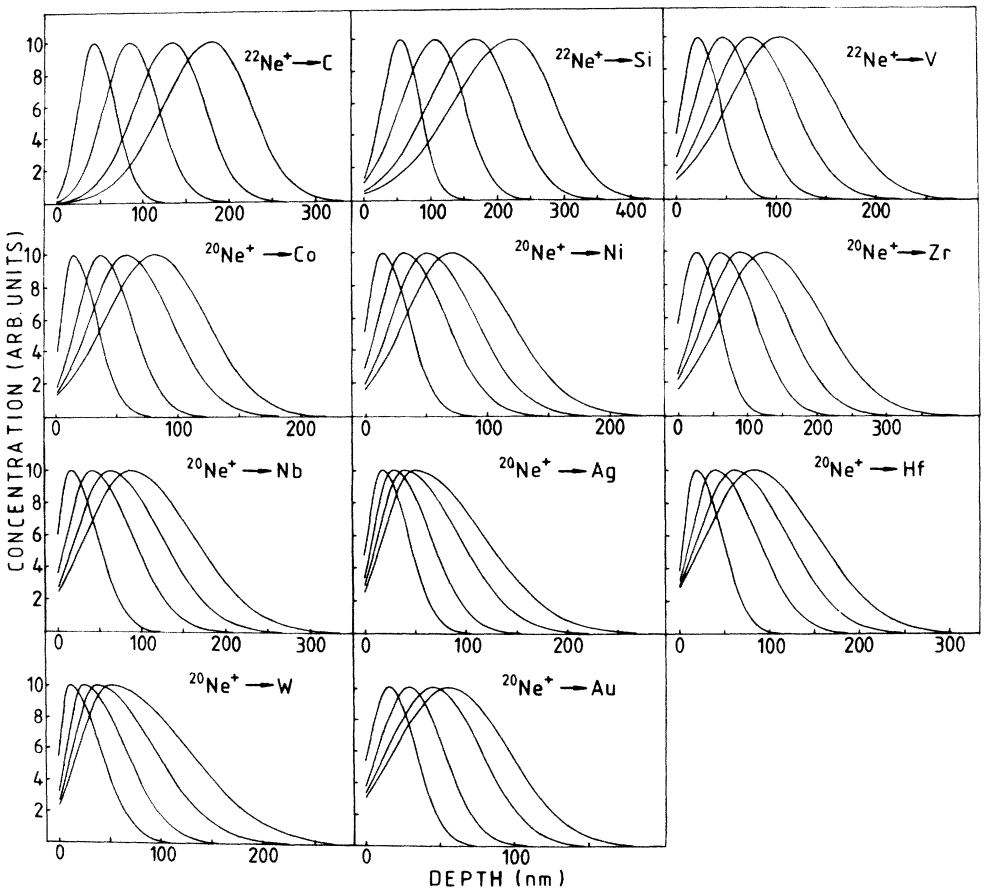

FIG. 3. The experimental, normalized neon concentration profiles for all measured backings. Each of these split-Gaussian concentration profiles were obtained by the least-squares fit of the yield calculated for a given split-Gaussian profile to the measured yield curve.

TABLE I. Ranges of $^{20}Ne^+$ and $^{22}Ne^+$ ions in 11 elements compared with calculated values. Values given do not include the sputtering corrections, see text.

Backing	Ion	Energy (keV)	$\hat{R}_{obs}$[a] (nm)	$\hat{R}_{amorph}$ (nm)	$\hat{R}_{poly}$ (nm)	$\overline{R}_{obs}$ (nm)	$\overline{R}_{obs}/\overline{R}_{amorph}$[a]	$\overline{R}_{obs}/\overline{R}_{poly}$	$\overline{R}_{PRAL}$ (nm)
C	^{22}Ne	25	41±3	40	37	49	1.27±0.12	1.15	41
		50	84±5	86	81	87	1.11±0.08	1.03	83
		75	134±7	132	123	129	1.10±0.06	1.03	125
		100	180±8	179	166	171	1.09±0.05	1.04	167
Si	^{22}Ne	25	54±4	51	41	57	1.14±0.11	1.04	50
		50	108±6	108	88	103	1.04±0.07	0.95	100
		75	169±8	166	141	156	1.05±0.05	0.99	151
		100	225±10	222	193	204	1.04±0.04	0.97	203
V	^{22}Ne	25	22±2	26	21	29.0	1.04±0.11	0.79	26.0
		50	47±3	58	45	53	0.99±0.06	0.83	51
		75	75±4	88	67	80	1.01±0.05	0.86	77
		100	105±5	120	91	109	1.04±0.04	0.92	104
Co	^{20}Ne	25	13±2	18	16	22.5	1.17±0.13	0.93	17.5
		50	36±2	37	33	42	1.17±0.07	0.99	34
		75	57±3	60	52	65	1.20±0.05	1.04	52
		100	81±4	82	68	84	1.18±0.04	1.04	69
Ni	^{20}Ne	25	14±2	17	16	24.3	1.29±0.13	0.86	16.9
		50	32±2	38	33	43	1.21±0.08	0.89	33
		75	50±3	60	51	62	1.19±0.06	0.93	50
		100	71±3	78	68	81	1.18±0.05	0.95	67
Zr	^{20}Ne	25	29±3	25	30	39	1.13±0.12	0.90	28
		50	63±4	62	58	76	1.20±0.06	0.99	55
		75	92±5	98	88	106	1.12±0.05	0.96	82
		100	128±6	131	108	143	1.19±0.04	1.08	110
Nb	^{20}Ne	25	15±2	22	21	33	1.23±0.12	0.81	21.6
		50	40±2	47	41	61	1.26±0.06	0.96	42
		75	61±3	76	64	84	1.20±0.05	0.92	62
		100	87±4	103	85	110	1.32±0.05	0.99	83
Ag	^{20}Ne	25	18±2	17	18	29.3	1.24±0.14[b]	0.86	18.6
		50	28±2	38	38	45	1.04±0.08[b]	0.79	36
		75	39±3	61	58	65	1.04±0.07[b]	0.85	53
		100	49±3	80	74	82	1.02±0.06[b]	0.84	71
Hf	^{20}Ne	25	18±2	22	21	32	1.11±0.11	0.85	18.5
		50	39±2	42	40	59	1.18±0.06	0.99	35
		75	61±3	62	61	81	1.16±0.05	0.96	51
		100	82±4	81	82	103	1.16±0.04	0.98	68
W	^{20}Ne	25	10±2	15	16	29.1	1.47±0.12	0.84	12.7
		50	24±2	30	29	46	1.33±0.07	0.85	23.9
		75	37±2	42	45	66	1.40±0.06	0.91	35
		100	51±3	57	62	90	1.46±0.06	1.02	47
W	^{22}Ne	25	9±2	14	14	26.7	1.40±0.10	0.78	12.7
		100	46±3	58	60	88	1.46±0.05	1.00	47
Au	^{20}Ne	25	16±2	16	16	22.3	1.07±0.12[c]	0.72	13.1
		50	30±2	30	30	35	0.98±0.08[c]	0.72	24.4
		75	46±3	46	43	51	1.02±0.06[c]	0.79	36
		100	57±4	62	57	64	1.00±0.06[c]	0.79	48

[a]Error limits include the experimental resolution and the error limits of the proton stopping power. Statistical error limits of the theoretical mean values are 0.6–1.5 %.

[b]Values corrected for sputtering are 1.49, 1.27, 1.26, and 1.25.

[c]Values corrected for sputtering are 1.28, 1.19, 1.22, and 1.20.

TABLE II. Standard deviations σ and reflection coefficients of $^{20}Ne^+$ and $^{22}Ne^+$ ions in 11 elements extracted from the experimental data and from the Monte Carlo calculations. Values given do not include the sputtering corrections, see text.

Backing	Density (g/cm^3)	Ion	Energy (keV)	σ_{obs} (nm)	σ_{amorph} (nm)	$\sigma_{obs}/\sigma_{amorph}$	Reflection coefficient (%)
C	2.3	^{22}Ne	25	21	13	1.57	0
			50	31	24	1.29	0
			75	40	34	1.18	0
			100	50	41	1.22	0
Si	2.33	^{22}Ne	25	27	22	1.20	0.5
			50	44	38	1.15	0.4
			75	60	54	1.12	0.2
			100	74	69	1.07	0.2
V	5.8	^{22}Ne	25	17	14	1.20	3.8
			50	28	25	1.13	2.6
			75	38	34	1.12	2.4
			100	50	43	1.15	2.2
Co	8.9	^{20}Ne	25	14	10	1.39	5.2
			50	22	17	1.24	4.0
			75	32	24	1.31	3.5
			100	39	30	1.31	2.6
Ni	8.9	^{20}Ne	25	16	10	1.59	5.5
			50	25	17	1.47	4.4
			75	32	24	1.37	3.3
			100	40	30	1.34	3.0
Zr	6.49	^{20}Ne	25	24	19	1.26	11.5
			50	40	33	1.23	9.0
			75	54	45	1.22	8.0
			100	70	57	1.22	6.5
Nb	8.55	^{20}Ne	25	22	15	1.49	11.9
			50	36	25	1.43	9.5
			75	47	34	1.40	8.4
			100	59	44	1.36	6.8
Ag	10.5	^{20}Ne	25	18	14	1.36	14.7
			50	27	23	1.20	11.0
			75	39	31	1.26	8.9
			100	49	38	1.27	7.9
Hf	13.1	^{20}Ne	25	20	16	1.24	23.0
			50	34	27	1.27	19.0
			75	46	37	1.23	17.3
			100	57	45	1.26	14.7
W	19.3	^{20}Ne	25	20	11	1.82	21.8
			50	29	18	1.57	19.0
			75	40	25	1.59	16.4
			100	53	31	1.69	14.8
W	19.3	^{22}Ne	25	18	11	1.69	21.9
			100	54	32	1.71	14.4
Au	19.3	^{20}Ne	25	14	12	1.16	25.1
			50	20	19	1.02	20.5
			75	28	26	1.06	19.2
			100	34	33	1.03	17.0

ly before the slowing down of each ion), and random (the crystal is rotated after each collision). In the crystalline cases, the following crystalline structures are assumed for backings: fcc for Ni, Ag, and Au; bcc for V, Nb, and W; hcp for C (an elongated hcp structure of graphite[20]), Co, Zr, and Hf; diamond structure for Si. After each collision in the crystal, the next scatterer was chosen in the fcc, bcc, and hcp structures from the nearest and next nearest

neighbors to be the one with the smallest impact parameter. In the case of silicon and graphite, the next scatterer was the atom that was nearest and had an impact parameter less than $b_{max}=1.2$ and 1.5 Å, respectively. With the above-mentioned parameters the random and amorphous structures yielded distributions of practically the same shape. However, the random simulations for different crystalline structures seemed to have a systematic tendency to give range values typically 5% greater than those for amorphous materials. Similar results were obtained in the comparison of simulations with TRIM (amorphous target) and MARLOWE (crystalline target).[21] The mean ranges by the PRAL algorithm are clearly shorter than the simulated ones for amorphous structure, especially in heavy backings, mainly because the reflection of the incident ions is not included in the PRAL calculations.

The total reflection coefficients, i.e., the reflected particles as a percentage of the total number of incident particles, obtained from the Monte Carlo simulations, are given in the last column of Table II. The values are averages of calculations for the amorphous and polycrystalline structures. The reflection coefficient for a polycrystalline target structure seemed to be typically 10–15% lower than for the corresponding amorphous one. Comparison of the depth distributions and reflection coefficients in amorphous and random structures simulated for gold using computer codes TRIM and MARLOWE indicated differences in the same direction as here both for range values and reflection coefficients.[21]

The measured and calculated range profiles of 50-keV Ne^+ ions are compared in Fig. 4. It can be seen that the predictions, neither for the amorphous nor the polycrystalline structure, agree well with the experimental profile, but the experimental distribution is somewhere between these two extremes. This is to be expected due to defects in the backing. It should be kept in mind that in these calculations, the erosion of the surface due to the implanted atoms is not included, although this has a noticeable effect on the neon distributions obtainable in "soft" metals as is discussed in the following section. This is clearly seen in the case of silver, which has the highest sputtering ratio of the backings used in this work.

B. Effect of sputtering and implanted dose

During implantation and profile measurements, several physical effects, e.g., sputtering, diffusion, and surface contamination, can cause systematic errors in the experimental results. Especially with inert-gas implants, sputtering of the surface is the most important unavoidable effect of high-fluence implantations. In the following, sputtering corrections for the measured range parameters are estimated on the basis of the model outlined by Schulz and Wittmaack.[22]

Since the sputtering yield of an ion can depend on several physical quantities (e.g., target temperature, surface topography, and the removed layer thickness), simplifying assumptions are needed to get rough estimates. If the sputtering yield for a certain ion-target combination at fixed implantation energy is assumed to be constant, e.g., independent of fluence, the total thickness sputtered d is given by

$$d=\Phi S/n_0 \ . \tag{1}$$

Here, Φ is the total implanted fluence, S is the sputtering yield (atoms/ion), and n_0 is the atomic density of the target. If $C_0(x)$ is the normalized range distribution in the absence of sputtering, the distribution affected by sputtering is obtained from

$$C(x,\Phi)=\frac{1}{d}\int_0^{d(\Phi)} C_0(x+y)dy \ . \tag{2}$$

The effect of sputtering on range parameters can be calculated using this formula either numerically or by deriving analytical expressions for an assumed function distribution, e.g., the predicted shift of the modal range of a split-Gaussian distribution can be obtained from a simple formula:

$$\Delta\hat{R}_s=d/(1+\sigma_+/\sigma_-) \ . \tag{3}$$

The sputtering yields for Ne^+ ions on the targets used in the present work were taken either from the experimental results or from the theoretical calculations.[23] The sputtering yields are given, in Table III, at 45 keV, since this was the bombarding energy used in most of the experimental studies. The yield values for the bombarding energies used were obtained using the theoretical energy dependence of backward sputtering at normal incidence.[24] When inelastic effects on the sputtering yield can be ignored, the energy dependence of backward sputtering yield is the same as that of the nuclear stopping power. The corrections $\Delta\hat{R}_s$ for experimental modal ranges calculated using Eq. (3) are given for the 25- and 100-keV values in Table III. The $\Delta\hat{R}_s$ values for the modal ranges of 50- and 75-keV $^{22}Ne^+$ ions in C, Si, and V are almost the same as the values for 25- and 100-keV implantations. This is due to the fact that the fluences were 2.5×10^{16} Ne^+ ions/cm^2 for the 25- and 50-keV and 3.2×10^{16} Ne^+ ions/cm^2 for the 75- and 100-keV implantations. However, since the fluences of the ^{20}Ne implantations were 2.5×10^{16}, 3.1×10^{16}, 5.0×10^{16}, and 6.2×10^{16} Ne^+ ions/cm^2 for 25, 50, 75, and 100 keV, respectively, the corrections for the 50- and 75-keV values for ^{20}Ne can be obtained from the 25- and 100-keV values by linear interpolation. It can be concluded that the corrections $\Delta\hat{R}_s$, excluding values for Ag and Au, are of the same order or less than the error limits of $\hat{R}$ values given in Table I.

The sputtering corrections of mean ranges calculated using Eq. (2) are 0.6–1.0 times the corrections for modal values, depending on the shape of the distribution. For all targets used, except Ag and Au, the sputtered-layer thickness is less than 50% of the standard deviation of the range profile simulated for amorphous structure. Thus, in these cases, the increase in the width of the profile is less than about 2% and so the σ values given in Table II are only slightly affected. The increase in the width for Ag and Au profiles is 8–10 and 6–8%, respectively.

It is worthwhile to note that the possible change of sputtering yield with the thickness of the removed layer can significantly affect the sputtering corrections. Although this kind of change has not been investigated systematically for different materials, such a strong dose

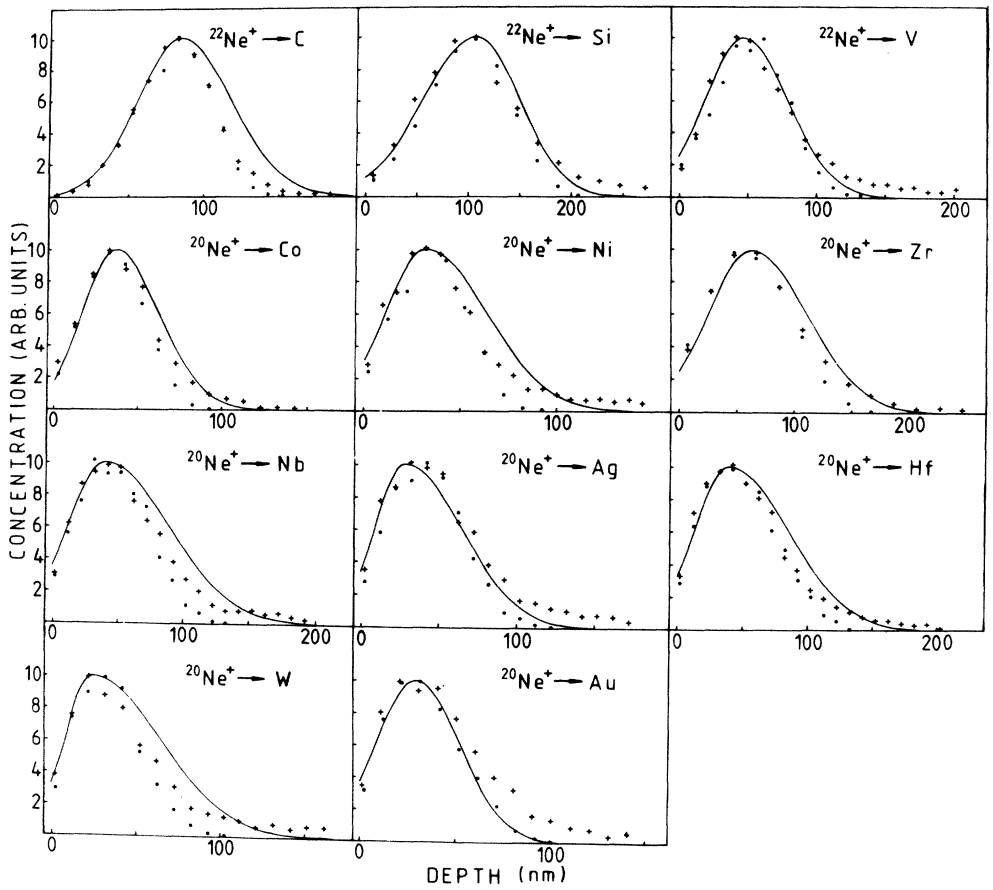

FIG. 4. The experimental 50-keV neon concentration profiles (solid lines) compared with the Monte Carlo simulations for amorphous (●) and polycrystalline (+) structures of backings. In each simulation, typically, 3000 incident particle histories were calculated.

TABLE III. The corrections for experimental modal-range values due to the sputtering of target surface during implantation.

Backing	Sputtering yield at 45 keV (atoms/Ne ion)	$\Delta\hat{R}_s$ for 25 keV Ne distribution (nm)	$\Delta\hat{R}_s$ for 100 keV Ne distribution (nm)
C	0.3[a]	0.4	0.3
Si	0.85[b]	2.4	2.3
V	0.3[c]	0.5	0.5
Co	1.35[d]	1.4	3.7
Ni	1.4[c]	1.5	3.3
Zr	1.2[d]	3.6	6.7
Nb	1.2[d]	1.8	4.7
Ag	4.5[c]	8	26
Hf	0.6[d]	1.1	3.2
W	1.0[c]	1.8	2.8
Au	3.5[e]	7	20

[a]Theoretical value from Ref. 23.
[b]Experimental value from Ref. 28.
[c]Experimental value from Ref. 25.
[d]Estimate based on the general systematics of experimental data in Refs. 23 and 25.
[e]Experimental value from Ref. 29.

dependence has been found for several metals (e.g., Cu, Ag, and Au)[25–27] and silicon.[28] Low-dose values were observed to be less than the high-dose values for Ag (25% increase)[25] and silicon.[28] The opposite behavior was found for sputtering of Au with different ions.[29]

It can be concluded that in the present work, the effect of sputtering on the profile was found to be a shift towards the surface and a slight increase in width. As compared to the modal-range values from the simulations for amorphous and polycrystalline materials, the corrected modal ranges are generally very close to the ones calculated for the amorphous structure or somewhere between these two theoretical estimates. The corrected experimental mean ranges are 0.85–1.05 of the theoretical values for polycrystalline materials and are longer than the ones for amorphous structure by a factor of 1.1–1.3. Judging from the range systematics of the other targets in Table I, the sputtering corrections for mean values of the more sputtered targets Au and Ag are reasonable, see remarks in Table I.

In general, profiles of inert gases in many backing materials are observed to be very stable, with regard to both time and temperature.[25] Diffusion processes or surface peak formation during the implantations were not observed in the present study.

Dose effects were studied in the case of tungsten, where the deviations of experimental profiles from the ones calculated assuming amorphous structure are largest. For this purpose a series of samples were implanted with 6.2×10^{14}, 6.2×10^{15}, and 3.1×10^{16} $^{22}Ne^+$ ions/cm^2 for 25-keV and 1.2×10^{15}, 1.2×10^{16}, and 6.2×10^{16} $^{22}Ne^+$ ions/cm^2 for 100-keV. It turned out that the 851.4-keV resonance of the reaction $^{22}Ne(p,\gamma)^{23}Na$ could not be used for accurate profiling of the low-dose implants due to the disturbing γ yield from the reaction $^{19}F(p,\alpha\gamma)^{16}O$ on the trace content of fluorine in the surface layer of the targets. The γ-ray yield from the strong, broad ($\Gamma=4.5$ keV) resonance in the $^{19}F(p,\alpha\gamma)^{16}O$ reaction at $E_p=872$ keV disturbed the measurements, particularly in the tails of the distributions. Therefore, the 640-keV $^{22}Ne(p,\gamma)$ resonance was used for these profiles. Using this resonance, the background γ yield from fluorine was reduced several orders of magnitude as compared with the upper resonance and it was no longer a serious source of error. The shapes of the profiles for different doses turned out to be the same within statistical error limits. The ^{20}Ne and ^{22}Ne doses used in the range measurements were in the region studied for tungsten and the implanted atom concentration was always less than ~10 at. %. Hence it is probable that sputtering is the only dose-dependent effect that gives observable changes in measured profile shapes.

V. DISCUSSION

As mentioned earlier, the sputtering-corrected modal ranges agree rather well with the predictions for amorphous materials. However, as can be seen from Fig. 4 and as can be expected *a priori* on the basis of the crystallinity of the backings, the experimental profiles have somewhat longer tails than the ones simulated for amorphous structure. Accordingly, the experimental mean-range values are higher than the results assuming amorphous backing, by a factor of 1.1–1.3 and a similar difference is seen in the standard deviations σ of these profiles in Table II. In fact, the ratios $\bar{R}_{\rm obs}/\bar{R}_{\rm amorph}$ and $\sigma_{\rm obs}/\sigma_{\rm amorph}$ are well correlated ($r=0.93, p<0.005$), as is to be expected. The reasons for the differences between the experimental and theoretical results are discussed below.

The appearance of long tails in measured dopant profiles not reproducible with simulations for amorphous structure is a rather well-known phenomenon. Several effects, such as channeling phenomena in the microcrystalline material, diffusion processes and atomic mixing and knock-on effects have been suggested to account for the discrepancy between theoretical calculations and experiments.[30] The effect of the structure of the backing is also clearly demonstrated in Fig. 4. Although the amorphization processes during high-dose implantations have been studied in a few special cases, there is no adequate model to predict the degree of amorphization for a certain ion-target combination, especially in the case of metal backings. As a rule of thumb, based on the experimental data, the crystalline structure converts to the amorphous one in semiconductors and in a number of alloys and intermetallic compounds, even at low doses. For example, the critical dose for amorphization of silicon with 40-keV phosphorus implantation at room temperature is about 5×10^{14} P^+ ions/cm^2.[31] The corresponding value for Ne can be expected to be well below 10^{16} ions/cm^2 according to the systematics of the critical doses for different ions in silicon.[31] The doses used here for silicon, i.e., 2.5×10^{16} and 3.1×10^{16} Ne^+ ions/cm^2, are above this limit and accordingly, the experimental results agree well with the simulations for amorphous structure. In contrast to semiconductors, elemental metals are found to remain crystalline, as a large proportion of the defects produced anneal out even during room-temperature implantation.[32] As an exception for metals, gallium was recently amorphized by Ne- and Ar-ion irradiation at low temperatures (<10 K).[33] In addition to the irradiation-induced effects, amorphous metallic phases can be produced in some cases with appropriate implants (e.g., B, P, Si, As) into metals,[34] even at low concentrations (<10 at. %). In conclusion, no significant amorphization can be expected to occur in metals by implantation with chemically inert neon in this study. However, damage and distorsion of lattice caused by neon irradiation and possible neon bubbles[35] can behave like a nominal amorphous material.

In the present study, the simulations assuming polycrystalline material clearly overestimate the experimental profiles in the tails. The absence of these deeply channeled particles in the experimental profiles is evidently due to the fact that the assumptions used in simulations do not hold true in the experimental situation. In the simulation for polycrystalline structure, it is assumed that each ion enters into a perfect, randomly oriented crystal and slows down in this single grain. Due to damage in the crystal, a proportion of the channeled ions stop earlier than in simulations resulting in broader distribution than the simulated one. In addition to crystalline defects,

channeling can be either decreased or increased, depending on the incident direction, by even small quantities of surface impurities,[36,37] e.g., the native oxide layer characteristic of several metals and silicon. The orientation effect of the surface was studied in the case of tungsten by measuring the profile at different angles. However, no change was observed. Furthermore, the partial orientation of grains allowed, e.g., in the [100] direction simulated for tungsten, gave even larger tails than in the case of a normal polycrystalline material and could not reproduce the larger width of the experimental profile.

The small differences between the measured and both the simulated profiles can be attributed to two additional factors. Firstly, the width of a distribution is a second-order effect and is difficult to measure as accurately as the mean value. When using the NRB method for profiling, the width depends on the straggling of the probing proton beam. This is estimated reasonably well[15] in light elements by Vavilov's theory and such analytical formulae as that of Lindhard and Scharff,[38] although an oscillatory dependence on Z_2 is evidently present. Secondly, Z_2 oscillations of the electronic stopping power of neon can cause a shift in the theoretical profiles, since at the implantation energies used, both the electronic and nuclear stopping power affect the range profile. This correction factor cannot, however, produce the long tails for profiles simulated for amorphous structure. Especially, for 25-keV Ne profiles, where the experimental resolution is best in this case, the electronic stopping correction factor has only a minor effect on the profile. Furthermore the ratios $\overline{R}_{\text{obs}}/\overline{R}_{\text{amorph}}$ given in Table I did not seem to follow accurately the general systematics of Z_2 oscillation for light ions.[39]

Powers and Whaling measured the ranges of several ions, e.g., N and Ne, in Be, B, C, and Al for incident ion energies of 50—500 keV by proton elastic scattering.[40] Their results for neon ranges in C, 77.8 ± 9.1 nm at 50.1 keV and 166.5 ± 11.7 nm at 99.6 keV, agree with the present results within the error limits. Switkowski *et al.*[41] did not extract exact numbers from their γ-ray yield curves for neon in silicon. But, as they concluded, their results for 30—150-keV Ne implantations are consistent with the calculations for amorphous silicon in agreement with the present results. A further comparison is made with the range systematics of ^{15}N (Refs. 7 and 8) and ^{27}Al (Ref. 9) in metals, studied in our laboratory. The present results agree reasonably with the ^{15}N data, where the ratio $\overline{R}_{\text{obs}}/\overline{R}_{\text{amorph}}$ varied from 0.9 to 1.4 to be compared with the present values of 1.1—1.3. However, the agreement is much better than for ^{27}Al, where the $\overline{R}_{\text{obs}}/\overline{R}_{\text{amorph}}$ values as high as 1.6—1.7 were obtained.

[1] J. F. Ziegler, J. P. Biersack, and U. Littmark, *The Stopping and Range of Ions in Solids*, (Pergamon, New York, 1985), Vol. 1.

[2] M. Hautala, Phys. Rev. B **30**, 5010 (1984).

[3] M. T. Robinson and I. M. Torrens, Phys. Rev. B **9**, 5008 (1974).

[4] H. H. Andersen, *Bibliography and Index of Experimental Range and Stopping Power Data*, Vol. 2 of *The Stopping Power and Ranges of Ions in Matter* (Pergamon, New York, 1977).

[5] A. Anttila, M. Bister, A. Fontell, and K. B. Winterbon, Radiat. Eff. **33**, 13 (1977).

[6] L. C. Feldman and S. T. Picraux, in *Ion Beam Handbook for Material Analysis*, edited by J. W. Mayer and E. Rimini (Academic, New York, 1977), p. 112.

[7] M. Luomajärvi, J. Keinonen, M. Bister, and A. Anttila, Phys. Rev. B **18**, 4657 (1978).

[8] A. Anttila, R. Paltemaa, T. Varjoranta, and R. Hentelä, Radiat. Eff. **86**, 179 (1984).

[9] J. Keinonen, M. Hautala, M. Luomajärvi, A. Anttila, and M. Bister, Radiat. Eff. **39**, 189 (1978).

[10] P. Eichinger and H. Ryssel, in *Ion Implantation Techniques*, edited by H. Ryssel and H. Glawischnig (Springer-Verlag, Berlin, 1982), p. 255.

[11] P. M. Endt and C. van der Leun, Nucl. Phys. A **214**, 1 (1973).

[12] A. Anttila and M. Hautala, Appl. Phys. **19**, 199 (1979).

[13] R. Lappalainen (unpublished).

[14] P. V. Vavilov, Zh. Eksp. Teor. Fiz. **32**, 920 (1957). [Sov. Phys.—JETP **5**, 749 (1957)].

[15] G. Deconninck, *Introduction to Radioanalytical Physics* (Akademiai Kiado, Budapest, 1978), p. 64.

[16] J. F. Gibbons and S. Mylroie, Appl. Phys. Lett. **22**, 568 (1973).

[17] H. H. Andersen and J. F. Ziegler, *Hydrogen Stopping Powers and Ranges in All Elements* (Pergamon, New York, 1977).

[18] J. P. Biersack, Z. Phys. A **305**, 95 (1982).

[19] M. Bister, M. Hautala, and M. Jäntti, Radiat. Eff. **42**, 201 (1979).

[20] R. W. G. Wyckoff, Crystal Structures, (Interscience, New York, 1963), Vol. 1, p. 26.

[21] W. Eckstein, H. Verbeek, and J. P. Biersack, J. Appl. Phys. **51**, 1194 (1980).

[22] F. Schulz and K. Wittmaack, Radiat. Eff. **29**, 31 (1976).

[23] H. H. Andersen and H. L. Bay, in *Sputtering by Particle Bombardment I*, Vol. 47 of *Topics in Applied Physics*, edited by R. Behrisch (Springer-Verlag, Berlin, 1981), p. 145.

[24] P. Sigmund, Phys. Rev. **184**, 383 (1969).

[25] O. Almen and G. Bruce, Nucl. Instrum. Methods **11**, 257, (1961); **11**, 279 (1961).

[26] H. H. Andersen and H. L. Bay, Radiat. Eff. **13**, 67 (1972).

[27] H. H. Andersen, Radiat. Eff. **19**, 257 (1973).

[28] H. H. Andersen and H. L. Bay, J. Appl. Phys. **46**, 1919 (1975).

[29] H. H. Andersen and H. L. Bay, J. Appl. Phys. **46**, 2416 (1975).

[30] M. Hautala, Radiat. Eff. **51**, 35 (1980).

[31] H. Ryssel and I. Ruge, *Ionenimplantation* (Teubner, Stuttgart, 1978).

[32] D. M. Follstaedt, Nucl. Instrum. Methods **B7/8**, 11 (1985).

[33] M. Holz, P. Ziemann, and W. Buckel, Phys. Rev. Lett. **51**, 1584 (1983).

[34] W. A. Grant, Nucl. Instrum. Methods **182/183**, 809 (1981).

[35] N. Marachov and P. J. Goodhew, Radiat. Eff. Lett. **85**, 61 (1984).

[36]E. V. Kornelsen, F. Brown, J. A. Davies, and G. R. Piercy, Phys. Rev. **136**, A849 (1964).
[37]M. Hautala, Nucl. Instrum. Methods B **15**, 75 (1986).
[38]J. Lindhard and M. Scharff, Mat. Fys. Medd. Dan. Vid. Selsk. **27**, no. 15 (1953).
[39]D. Fink, J. P. Biersack, M. Städele, K. Tjan, and V. K. Cheng, Nucl. Instrum. Methods **218**, 817 (1983).
[40]D. Powers and W. Whaling, Phys. Rev. **126**, 61 (1962).
[41]Z. E. Switkowski, J. C. Overlay, Shiu-Chin Wu, C. A. Barnes, and J. Roth, J. Nucl. Mater. **78**, 64 (1978).